Density of States Effective Mass for p-Type Mg_2Si-Mg_2Sn Solid Solutions: Comparison between Experiments and First Principles Calculations

Johannes de Boor[,1], Alexandre Berche[2] and Philippe Jund[*,2]*

[1] Institute of Materials Research, German Aerospace Center (DLR), 51147 Koeln, Germany
E-mail: Johannes.deboor@dlr.de

[2] ICGM, Univ. Montpellier, CNRS, ENSCM, Montpellier, France

E-mail: Philippe.Jund@umontpellier.fr

Abstract

Tailoring and further optimization of thermoelectric materials requires detailed knowledge and understanding of the thermal and electrical transport in these materials. One crucial parameter is the density of states effective mass, which governs both the electrical conductivity as well as the Seebeck coefficient. We investigate the density of states effective mass for magnesium silicide, magnesium stannide and their solid solutions using experimental data as well as Density Functional Theory in a Generalized Gradient Approach; for the solid solutions, the Special Quasi-Random Structures approach is employed. Extracting the effective mass directly from the calculated densities of states we can show an approximatively linear decrease from Mg_2Si to Mg_2Sn and consistency with respect to the chosen cell size. The experimental data, obtained assuming a single parabolic band model, shows good agreement with the calculated data for Mg_2Sn and Sn-rich solid solutions, but a clear difference at the Si-rich side. The lower effective mass for the Sn-rich solid solutions indicates that the electronic properties are expected to be superior to those of Si-rich solid solutions as long as minority carrier effects can be neglected.

Introduction

Thermoelectric generators (TEG) can convert heat directly into electrical energy and have advantages such as small system size, no moving parts, environmental compatibility and high reliability. The development of thermoelectric generators is promising for a range of diverse applications, ranging from self-powering sensors to waste heat recovery in the automotive sector and the steel industry to the powering of space probes[1-2]. The efficiency of thermoelectric generators depends on the figure of merit zT of the employed materials which is given by $zT = \frac{S^2\sigma}{\kappa} T$, where S is the Seebeck coefficient, σ the electrical conductivity, κ the thermal conductivity, and T the temperature.

The field of thermoelectrics has made significant progress recently due to the development of efficient thermoelectric materials with high zT [3 4 5 6 7]. Among the considered materials, magnesium silicide based solid solutions are highly promising for thermoelectric applications in the middle temperature range (300-800 K) due to materials abundance, non-toxicity, low density and cost, good environmental compatibility, and thermoelectric performance. While binary n-type Mg_2Si is a decent thermoelectric material with $zT_{max} \approx 0.8$ [8-12] the thermoelectric properties are significantly enhanced upon formation of a solid solution with Mg_2Sn: $zT_{max} \approx 1.4$ [13-19]. Even though solid solution formation was shown to be beneficial for the p-type system as well [20], the p-type properties are clearly inferior ($zT_{max} \sim 0.6$) and further optimization is highly desirable for a practical implementation of Mg_2Si-based thermoelectric generators. The progress, that has been achieved for p-$Mg_2(Si,Sn)$ over the last years [21] was due to improved synthesis techniques and the increase in experimentally achievable carrier concentrations due to the implementation of "new" dopants, in particular Li [22-23]. Further progress can be expected with deeper knowledge of the electronic band structure of the system, especially on the Si-rich side, where little experimental data is available [21]. Direct experimental characterization of the electronic (valence) band structure is rare [24] and often limited to the measurement of the large direct band gap in the system [25]. Instead, information on the valence bands is often obtained by modeling experimental data using single or multiband models. If the material system is sufficiently high doped, a single parabolic band model can be assumed and the density of states effective mass m_D^* can be obtained directly from a combined analysis of the experimentally measured transport properties. This has been done for several solid solutions of $Mg_2Si_{1-x}Sn_x$, usually for a fixed value of x [23, 26-28]. We have recently shown that the transport properties can be modeled using a single parabolic band (SPB) model for the whole solid solution and have extracted values for the effective mass as a function of composition x, however, experimental data on the Si-rich side is still missing [21]. On the other hand, if multi-band models are employed, the effective mass is usually used as input/fitting parameter [29-30]. These models usually contain a number of adjustable parameters which are partially interdependent in a complex manner. For this reason the accuracy of the thus obtained material parameters is limited and the conclusions on the band structure have a limited validity.

First principles calculations can provide independent insight on the electronic band structure, and due to its good thermoelectric properties, $Mg_2(Si,Sn)$ has been intensively studied using first principles calculations; most of the detailed analyses focus on the binaries. Bourgeois et al. calculated the electronic band structure of Mg_2Si and Mg_2Sn using a full potential linearized augmented plane wave approach [31]. They also compared different exchange correlation functionals and showed that the use of a modified Becke-Johnson (mBJ) functional leads to a much better

agreement of the calculated band gaps compared to the previously often employed generalized gradient (GGA-PBE) approaches. They also investigated the change of the electronic band structure upon dopant incorporation but their analysis of the effect of the Si:Sn ratio in the solid solution was limited. Kutorasinski et al. investigated the valence band structure of Mg_2Si, Mg_2Ge and Mg_2Sn in detail using a Green's functions approach and showed that the incorporation of relativistic effects changed the valence band properties significantly for Mg_2Ge and Mg_2Sn [32]. For these two compounds the so-called split-off (SO) band is shifted energetically down from the light (LH) and heavy hole (HH) bands playing thus only a minor role in the transport properties. They also introduced a simple way to extract the (density of states) effective mass directly from the density of states and showed that the curvature of the valence bands differs between Mg_2Si and Mg_2Sn, leading to a lower (density of states) effective mass for Mg_2Sn.

The band structure of solid solutions was studied by Pulikkotil [33] using GGA-mBJ and recently, Guerra et al., who employed Green's functions to calculate the electronic band structure of binaries and solid solutions in the Mg_2X (X=Si, Ge, Sn) system and furthermore calculated the (transport/inertia) effective mass along different crystallographic directions [34]. Their analysis showed a decrease of the hole effective mass with increasing Sn-content in $Mg_2(Si,Sn)$, but the obtained functional dependence is complex and surprising. However, they also found non-linearly varying lattice constants for the solid solutions in disagreement with all other calculations and experimental results (see e.g. [35-37]). As band structure and lattice constant are closely related this might explain their surprising results.

In this manuscript we use DFT-GGA to determine the structural properties of Mg_2Si, Mg_2Sn and solid solutions of these two. We furthermore employ a meta-GGA approach to calculate the electronic band structure of this material class. We focus on the valence bands here as these are mainly composed by the p-states of Si/Sn and are therefore expected to be stronger influenced by composition. While calculation schemes based on complex codes like BoltzTraP [38] directly yield the thermoelectric transport properties from the band structure, we find that calculation of the density of states effective mass as intermediate quantity is highly useful as it helps to rationalize the interplay between band structure and transport properties. We discuss a simple approach to extract the density of states effective mass directly from density of states and compare this to the experimental results obtained assuming a single parabolic band. We can show good agreement on the Sn-rich side but also find a clear disagreement on the Si-rich side of the solid solution series, possibly indicating limitations of the single parabolic band analysis.

Experimental

Li-doped $Mg_2Si_{1-x}Sn_x$ samples were prepared by high energy ball milling and current assisted sintering as described in an earlier work [20]. The sintering temperature was adjusted according to the sample composition [36] and is listed together with further parameters in Table 1. The material system is well known for a reported miscibility gap with disputed borders [39], but we showed recently that single phase synthesis is feasible [40] in agreement with other experimental reports [41-42]. The apparent discrepancy between experimental findings and calculation results might be related to a strain-induced suppression of the miscibility gap [43]. The temperature dependent measurements of the

Seebeck coefficient and electrical conductivity were performed using an in-house developed facility with a four-probe technique [44-45]. The room temperature Hall coefficient R_H for different samples was determined using an in-house facility with a van der Pauw configuration under varying magnetic field of maximum 0.5 T [46-47]. Based on periodic reference measurements and comparison with the NIST standard reference material 3451 and international round robin tests [48-50], measurement accuracy is given by ±5%,±5% and ±10% for S, σ, and R_{H}.

Calculation details

The DFT calculations were performed using the Vienna *ab initio* simulation package (VASP) [51-52] and the projector augmented waves (PAW) technique [53-54] within the generalized gradient approximation (GGA). The Perdew-Wang 91 parameterization (PW91) was applied [55]. Previous studies on Mg_2Si and Mg_2Sn have shown that the standard GGA underestimates the electronic band gap, predicting a semimetallic behavior for Mg_2Sn, see e.g. [33, 56]. To avoid this problem, the modified Becke-Johnson (mBJ) meta-GGA functional [57-58] has been used for the electronic properties.

Standard versions of the PAW potentials for Mg and Si were used while for Sn, the d semi-core states were treated as valence states. The used pseudo-potential names are respectively Mg, Si and Sn_d. Two electronic states were included in the valence shell for Mg ($3s^2$), four were taken for Si ($3s^23p^2$) and fourteen were taken for Sn ($4d^{10}5s^25p^2$).

For the solid solutions, the Special Quasi-Random Structures (SQS) [59] method has been used. The distribution of atoms was generated in a supercell using the ATAT software suite [60] to avoid artificial ordering effects in the distribution of the atoms. In this methodology, 15 cells were initially generated and the "less ordered" structure was selected as input file for the DFT calculations. Several supercells build from the primitive (P) or the conventional (C) cell have been used. They are named P111 (3 atoms, 1 formula unit), C111 (12 atoms), P222 (24 atoms) and P333 (81 atoms) in the present study.

The calculations were performed using the "high" precision setting in the VASP input file to avoid wrap-around errors. The first Brillouin zone has been integrated using Monkhorst-Pack k-point meshes. The reciprocal space mesh was set to obtain a high number of k-points in the irreducible part of the Brillouin zone depending on the size of the supercell: 19*19*19 for P111, 9*9*9 for C111 and P222 and 5*5*5 for P333. The cutoff energy was set to 500 eV for the whole study.

The calculated cell parameters were obtained by minimizing the total energy of the cells starting from the experimental structure. Both cell parameters and atomic positions have been relaxed. The convergence procedure stops when a difference in energy smaller than 1 µeV or a difference in force bellow 10 µeV/Å between two iterations was obtained.

For the density of states and effective mass calculations, the k-point mesh was strongly increased: 41*41*41 for P111, 23*23*23 for C111 and P222 and 11*11*11 for P333 supercell.

Results

Experimental

Nominal composition and relevant thermoelectric properties at room temperature of the samples are summarized in Table 1. For most of the samples, the full, temperature dependent thermoelectric data can be found in our recent work [20]. However the data for the sample with the composition $Mg_{1.98}Li_{0.02}Si_{0.5}Sn_{0.5}$ has been added as well as the analysis of the data for the samples with $x \leq 0.5$. It is worth mentioning that for $x \leq 0.5$ only one sample per composition has been analyzed. Note also that all the samples were found to be MgO free (on an XRD level) so that an influence of that on the transport analysis can be excluded [36]. In this publication we also reported a linear dependence of the lattice parameter on composition, indicating good agreement between nominal and actual Si/Sn ratio.

Table 1: Synthesis parameters and thermoelectric transport properties at room temperature obtained assuming a single parabolic band model.

Composition	T_{Sinter} [°C]	S [μV K^{-1}]	n_H [10^{20}cm^{-3}]	m_D^* [m_0]
$Mg_{1.98}Li_{0.02}Si$	800	581	0.013	3.8
$Mg_{1.98}Li_{0.02}Si_{0.8}Sn_{0.2}$	750	437	0.086	3.9
$Mg_{1.98}Li_{0.02}Si_{0.6}Sn_{0.4}$	750	247	0.41	2.5
$Mg_{1.98}Li_{0.02}Si_{0.5}Sn_{0.5}$	725	177	0.54	1.7
$Mg_{1.99}Li_{0.01}Si_{0.4}Sn_{0.6}$	700	165	0.51	1.45
$Mg_{1.98}Li_{0.02}Si_{0.4}Sn_{0.6}$	700	136	0.86	1.42
$Mg_{1.97}Li_{0.03}Si_{0.4}Sn_{0.6}$	700	126	1.01	1.53
$Mg_{1.99}Li_{0.01}Si_{0.2}Sn_{0.8}$	650	127	1.14	1.42
$Mg_{1.98}Li_{0.02}Si_{0.2}Sn_{0.8}$	650	94.4	1.36	1.19
$Mg_{1.97}Li_{0.03}Si_{0.2}Sn_{0.8}$	650	81.5	1.83	1.27
$Mg_{1.99}Li_{0.01}Sn$	600	87.7	1.44	1.13
$Mg_{1.98}Li_{0.02}Sn$	600	64.5	2.4	1.18
$Mg_{1.97}Li_{0.03}Sn$	600	65.2	2.6	1.22

While S is a measurement quantity, the carrier concentration n is obtained from the measured Hall coefficient R_H employing $n = \frac{r_H}{eR_H}$, where $r_{\mathrm{H}} = \frac{3F_{0.5}(\eta)F_{-0.5}(\eta)}{4F_0^2(\eta)}$ is the Hall scattering factor. It is a function of the reduced chemical potential $\eta = \frac{E_{\mathrm{F}}}{k_b T}$, ($E_{\mathrm{F}}$ is the Fermi energy, k_B Boltzmann's

constant) where $F_i\,(\eta)$ is the Fermi integral of order i $F_i = \int_0^\infty \frac{\epsilon^i d\epsilon}{1+Exp[\epsilon-\eta]}$. The reduced chemical potential was calculated from the Seebeck coefficient using $S = \pm\frac{k_b}{e}\left(\frac{2F_1(\eta)}{F_0(\eta)} - \eta\right)$, so that the density of states effective mass can be obtained from $n = 4\pi\left(\frac{2m_D^* k_b T}{h^2}\right)^{1.5} F_{\frac{1}{2}}(\eta)$ [61]. However, this analysis is only valid under the assumption that a single parabolic band is responsible for the thermoelectric transport in the material. That is generally assumed to be true for that material system [17, 20, 23, 62], if the charge carrier concentration is large enough. However, as can be seen from Table 1, the carrier concentration decreases with increasing Si-content, being partially below 10^{19} cm^{-3}. This phenomenon is observed consistently in literature [21] and possibly due to the interaction of dopants with intrinsic defects [63-64]. We have used a simple 2 band model to verify that the minority carrier impact is minor and a single band model can be applied, see supporting information.

Calculations

Figure 1 shows the evolution of the lattice constant for the binaries and various solid solutions with the Sn content x in $Mg_2Si_{1-x}Sn_x$. Depending on cell size we obtain $6.3588\ \text{Å} < a < 6.3592\ \text{Å}$ for Mg_2Si and $6.7994\ \text{Å} < a < 6.8046\ \text{Å}$ for Mg_2Sn (a table with all calculated lattice constants can be found in the SI). For the binary compounds, the calculated results agree well with previously published theoretical results with similar parameters. The cell parameters are very close to those calculated in GGA (PBE or PW91) for Mg_2Si [65-66] or Mg_2Sn [66]. Whatever the size of the supercell, the relaxed cell parameters describe a linear Vegard's law in the whole solid solution in agreement with the DFT calculations using LAPW [33] or PAW [66]. It should be noted that Guerra et al. [34] used the SQS methodology to describe the solid solution $Mg_2Si_{1-x}Sn_x$. However, with an LDA – KKR – CPA description they obtained a distinctly non-linear behavior of $a(x)$. Note that the linear trend observed here is consistent with basically all available experimental data [36, 67-68] and theoretical data [33, 39].

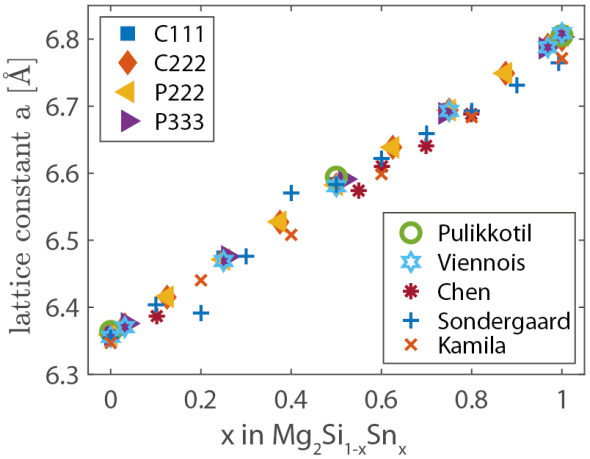

Figure 1: Calculated lattice constant (full symbols) for solid solutions of Mg_2Si-Mg_2Sn together with earlier theoretical (open symbols [33, 66]) and experimental work ('*' Chen2011 [67], '+' Sondergaard [67], 'x' Kamila [36])

Table 2 lists the calculated formation energies and values for the indirect band gap in Mg_2Si and Mg_2Sn. The energies of formation are in agreement with previous DFT calculations using GGA-PW91 on Mg_2Si [65]. Concerning the bandgap, we reproduce the values generally reported with mBJ in Mg_2Si [69]. The small difference for Mg_2Sn between our calculations and those of Brahim et al. [69] can be explained by the use of different pseudopotentials and exchange correlation methods. The obtained formation energies are somewhat lower than the experimentally obtained values. We found that the use of PW91 as exchange correlation functional results in lower formation energies (and thus closer to experimental values) compared to the more often used PBE functional.

As commonly observed [31] the use of GGA-DFT results in an underestimated band gap; for Mg_2Sn we find a semi-metallic behavior with a negative bandgap (defined as the difference in energy between the minimum of the conduction band and the maximum of the valence band). However, by employing the modified Becke-Johnson (mBJ) functional, we obtain positive band gaps for the binaries (and solid solutions) with absolute values comparable to previous calculations [33] and experiments. In detail, it should be mentioned that the bandgap calculated with mBJ, but using the linearized augmented plane-wave (LAPW) method rather than the PAW method, is similar for Mg_2Si (0.6eV[33] instead of 0.57eV) but significantly larger for Mg_2Sn (0.3eV [33] instead of 0.16eV). For the solid solutions we find that the supercell has to be large enough (around 70-80 atoms) to have a linear evolution of the gap with the composition. In this work, the spin-orbit interactions (SOI) have not been taken into consideration even if they are known to be significant for heavy atoms such as Sn (see Ref. [32] for example). Indeed, combining mBJ + SOI in Mg_2Sn calculations closes the bandgap of the compound to -0.004 eV. This shows that taking into consideration SOI for Mg_2Sn can be counterproductive since it gives a bad reproduction of the experimental bandgap. For this reason, SOI have not been included in the present calculations.

Table 2: Calculated parameters for Mg_2Si and Mg_2Sn (0K) together with experimental reference data .

Phase	Energy of Formation (eV/atom)		Bandgap (eV)		
	PW91	Exp	PW91	PW91-mBJ	Exp
Mg_2Si	-0.184	-0.22 to -0.31 [70-71]	0.221	0.57	0.66 to 0.78 [72-74] 0.77 [19, 75]
Mg_2Sn	-0.206	-0.26 to -0.28 [76]	-0.166	0.16	0.11 to 0.36 [77-80] 0.35 [19, 75]

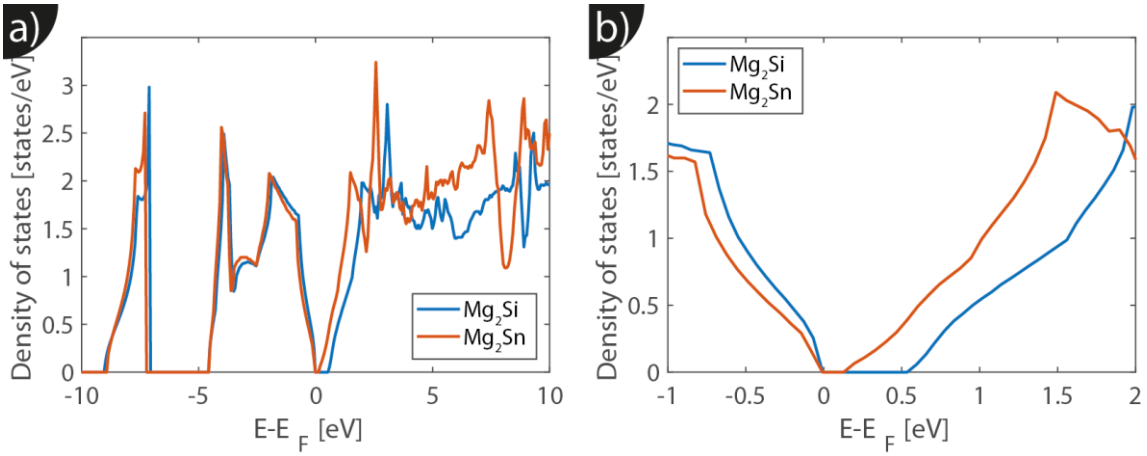

Figure 2: Calculated density of states for Mg_2Si and Mg_2Sn (P111, GGA-PW91+mBJ) and zoom-in in b) around the valence band edge

Figure 2 shows the calculated DOS for Mg_2Si and Mg_2Sn with a zoom-in around the valence band edge in b). DOS shape and values are quite similar for both valence band and conduction band comparing Mg_2Si and Mg_2Sn. The valence bands span roughly 5 eV, while the CB extent over a larger energy range, in agreement with previous calculations [31, 81-82]. We find good agreement of the VB-DOS with previous results [31, 81-82]. We also observe a different curvature of the VB-DOS close to the band edge for the two binaries, which determines mainly the transport properties and the m_D^*.

The carrier mobility μ is related to the transport (or inertia) effective mass m_I^* by $\mu = e\tau/m_I^*$. The most common way of calculating the transport effective mass of a compound consists in determining the curvature $E''(k)$ of the bands within the free electron model: m_I^* is then obtained following $m_I^* = \hbar^2/E''(k)$. For a material with a non-spherical Fermi surface the transport effective mass can be obtained by appropriate averaging of the masses along the principal axes of the effective mass tensor. For a material with an ellipsoidal Fermi surface it is given by $m_I^* = 3\left(\frac{1}{m_1^*} + \frac{1}{m_2^*} + \frac{1}{m_3^*}\right)^{-1}$, where m_1^*, m_2^* and m_3^* are the masses along the 3 main axes of the ellipsoid.

On the other hand the density of states effective mass m_D^* which governs the Seebeck coefficient is related to the single valley effective mass by $m_D^* = N_v^{2/3} m_b^*$ where N_v is the valley degeneracy. This single valley mass is related to the diagonal elements of the mass tensor $m_{1,2,3}^*$ by $m_b^* = (m_1^* m_2^* m_3^*)^{1/3}$. In consequence, both m_I^* and m_D^* govern the thermoelectric transport in a material. For $Mg_2(Si,Sn)$ solid solutions it has been shown that the Fermi surface is complex and not ellipsoidal [32] and the transport effective mass is therefore more complicated to determine. , It has been shown that the DOS can directly be used to calculate the density of states effective mass as shown in [32, 83]:

$$m_D^* = \frac{\hbar^2}{m_0}\sqrt[3]{\pi^4 D(E) D'(E)/V^2}$$	(1)

Here $D(E)$ and $D'(E)$ are the density of states and its derivate with respect to energy, V is the volume of the cell and m_0 is the free electron rest mass. Such density of states effective mass can easily be obtained experimentally from the measured Seebeck coefficient and carrier concentration

within the single parabolic band approximation as discussed in the experimental section. It is thus the experimentally better accessible quantity and can be used to test the calculation results.

Figure 3a) shows the DOS of the valence band and in b) the corresponding m_D^* is plotted. As Eq. (1) contains both D and D' direct implementation of the data results in a very noisy m_D^*. And while $D(E)$ can be fitted very well using polynomials, the resulting density of states effective mass shows unphysical dependence on energy, again because of the numerical interplay of $D(E)$ and $D'(E)$.

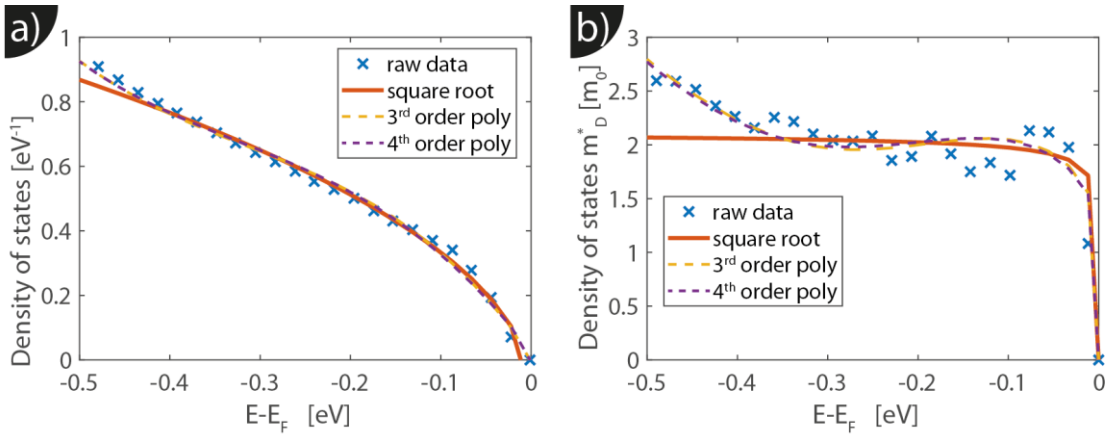

Figure 3: a): DOS, b): m_D^* of Mg_2Sn from a P111 cell. Raw data from the VASP calculation as well as several fits are shown.

We find that fitting the density of states to $D = A(E - E_F)^{0.5} + B$ with $B \approx 0$ allows for the most reliable calculation of m_D^* and for an estimation of the value close to the band edge. As for a bulk 3D crystal the density of states is supposed to show a square root dependence on energy in the free electron approximation, the choice of fitting function is physically motivated.

The m_D^* obtained from the square root fit depends only weakly on energy in the energy range close the valence band maximum and for a P111 cell of Mg_2Si we deduce $m_D^* = 1.95 \pm 0.05\ m_0$. The numerical error arises due to the ambiguities of the fitting procedure. Note also that the valence band maximum is not exactly at $E = 0\ eV$ but between $0\ eV$ and the numerical step width in energy, which corresponds to $0.01\ eV$ in our case. From the density of states effective mass obtained from the raw data and the polynomial fits, it can be seen that the density of states increases with decreasing energy, i.e. when going deeper into the valence band. This is presumably due to the non-parabolicity of the valence bands far from the VB maximum.

Similar calculations for Mg_2Sn yield $m_D^* \approx 1.40 \pm 0.05\ m_0$ and an increase with energy comparable to the results for Mg_2Si. Similarly, the density of states effective mass for the solid solutions of Mg_2Si and Mg_2Sn can be obtained. However, in the solid solutions one has to deal with an artificial lift of the degeneracy of the VB due to the break of symmetry induced by the varying tin content (see Supporting Info). This implies that m_D^* shows a step like increase until the contributions of the three valence bands have been totally taken into account. Therefore in order to obtain a correct DOS effective mass we have determined it at $E - E_F = -0.1\ eV$ (SI Fig S3) and deem the results obtained from the larger supercells as more reliable. It is worth mentioning that in some cases the shift of the SO band is so large that it is not reasonable to try to obtain m_D^* and compare it with experiments:

this is the case for x=0.375 in the P222 supercell (see SI Fig S3b)). Thus this composition has not been considered in the following discussion.

Figure 4 summarizes the calculated $m_D^*(E = -0.1\ eV)$ for various solid solutions of Mg_2Si and Mg_2Sn together with experimental data that is obtained assuming a single parabolic band model.

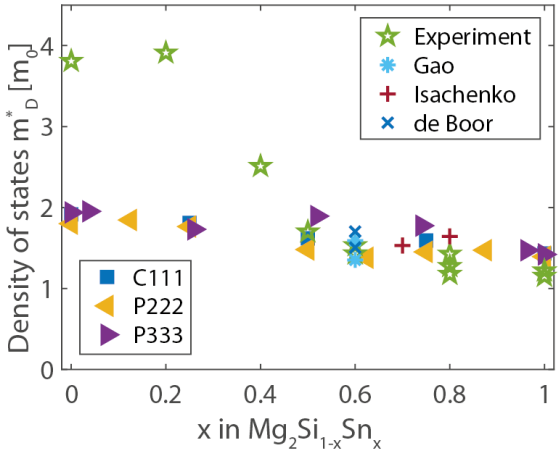

Figure **4: Comparison of calculated data for the density of states effective mass as well as the experimental results of this study and previous reports in $Mg_2Si_{1-x}Sn_x$ ('*' [84], '+' [85], 'x' [23]).**

The DFT results show decent agreement for the different cell sizes. According to the calculations, the density of states effective mass decreases approximately linearly from $2\ m_0$ for Mg_2Si to $1.4\ m_0$ for Mg_2Sn. The experimental results assuming SPB show a different behavior. For Mg_2Si the experimental result is almost double that of the DFT calculations and decreases rapidly around $x = 0.4$. For $x > 0.6$ the experimental results are slightly below the first principles results but show a similar dependence on composition. Note that the experimental data for m_D^* exhibits an increase with carrier concentration (see e.g. [27] or discussion in [21]), similarly to what we find numerically (Figure 3). Plotted in Figure 4 are however, the experimental results for different carrier concentrations, i.e. different chemical potentials, this explains partially the observed scatter in the experimental data. A further subtle difference between calculated and experimental data is that the calculated m_D^* is obtained from the electronic band structure of undoped Mg_2X, while the experimental data is (necessarily) obtained from samples whose carrier concentrations have been tuned by addition of a small amount of a non-isovalent element, for the data shown above mainly Li. However, calculation of the band structure with Li substitution shows no significant modification of the band structure - no defect band near the valence band edge - (see supporting information). Experimentally it was shown explicitly for $Mg_2Ge_{0.25}Sn_{0.75}$ that the behavior for several dopants (Li, Ga, Na) is similar as would be expected for a rigid band structure [22]. Comparative analysis of several experimental works did not find indications for non-rigid valence bands for the Sn-rich compositions [21]. Mg_2X is known for the relevance of intrinsic defects with respect to the electronic properties. However, while interstitials and vacancies are known to influence the carrier concentration, their influence on the density of states and hence m_D^* is minor [65].

While a single band approach is often used to analyze and predict the properties of p-type $Mg_2(Si,Sn)$, the existence of three distinct valence bands makes a multiband approach necessary for accurate predictions for the p-type as well as a correct modeling of the high temperature behavior of the n-type material [29, 86-88]. For this, the effective masses of the individual bands are a necessary input. These can be obtained by calculation of the band structure of the desired composition and a manual separation of the bands which is well feasible since in the reciprocal space the 3 VB don't cross. Each band is then integrated individually to obtain their contribution to the DOS. From the individual DOS, the single valley mass for each band can be obtained by applying Eq. (1) as outlined above.

The results for the three valence bands of Mg_2Si and Mg_2Sn are presented in Figure 5. Note that we use the labelling of the bands of Kutorasinski et al.[32]: heavy hole (HH), light hole (LO) and split-off band (SO), the later possessing the lowest m_D^*.

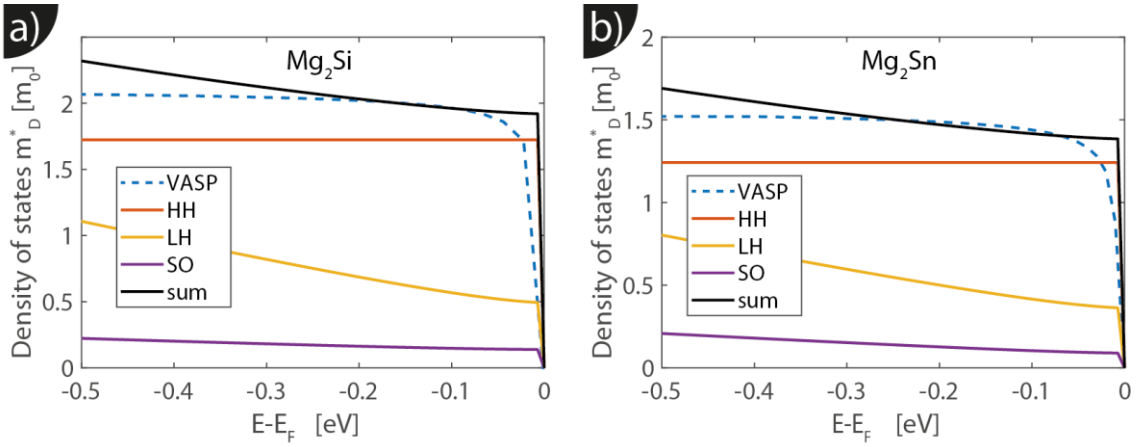

Figure 5: Density of states effective mass from the individual bands for Mg_2Si (a) and Mg_2Sn (b). The full lines show the effective mass of each band (and the sum), while the dashed line corresponds to the m_D^* obtained from the full DOS.

As expected, the HH band has the largest effective mass and as masses add up non-linearly $m_D^* = \left(\sum m_i^{*1.5}\right)^{2/3}$ it has by far the largest contribution to the total m_D^*, while the influence of the split-off band is negligible. It can also be deduced that the increase of $m_D^*(E)$ is mainly due to the energy dependence of the light band, while the heavy band shows a quite constant effective mass. Comparison of the m_D^* obtained from the total DOS and the addition of the individual band masses shows good agreement, supporting the chosen approach (the small differences are due to differences in the integration procedures). We also note that the effective mass ratio $m_{D,HH}^*/m_{D,LH}^* \approx 3.4$ is the same for Mg_2Si and Mg_2Sn, indicating that the band curvature of both sub-bands changes similarly for both bands with composition.

Discussion

Few other experimental data is available for highly doped p-type Si-rich $Mg_2(Si,Sn)$. Employing the same SPB analysis for Ga-doped $Mg_2(Si,Ge)$ from Ihou-Mouku et al., we find that those samples also

exhibit large values for the density of states effective mass: $2.8\ m_0 \leq m_D^* \leq 3.5\ m_0$ [89], similar to our results for Li-doped Mg_2Si.

For the binaries, we can compare our calculation results with those of Kutorasinski et al. Similar to us they also found a much smaller density of states effective mass for Mg_2Sn than for Mg_2Si. Quantitatively the results for Mg_2Si are comparable ($1.6\ m_0\ vs\ 2.0\ m_0$), however, for Mg_2Sn, their result ($\approx 0.5\ m_0$) is much smaller than our result ($1.4\ m_0$) and the experimental data ($1.1\ m_0$) [20, 32]. We also note that their result for the semi-relativistic calculation is closer to experimental values than the full relativistic calculation. The observed increase in $m_D^*(E)$ with decreasing Fermi level (going deeper into the valence band) has been observed experimentally as an increase with increasing hole concentration consistently for various compositions, see e.g. [20-21, 26-27, 90-91]. Shi and Kioupakis[92] have calculated the band structure for Mg_2Si and Mg_2Sn using DFT and many-body perturbation theory. They have calculated effective masses along certain crystallographic directions and also obtained density of states effective masses for the binaries using a hyperbolic fit function instead of a square root function [92]. While they also find a larger m_D^* for Mg_2Si, the absolute values ($m_D^*(Mg_2Si) \approx 0.9\ m_0$, $m_D^*(Mg_2Sn) \approx 0.6$) are relatively far from the experimental results.

Our DFT results of m_D^* for solid solutions of Mg_2Si and Mg_2Sn show an approximately linear decrease towards Mg_2Sn , in agreement with the experimental findings for $x > 0.5$ [20-21]. As discussed in previous reports, the valence bands are mainly composed of p-states of Si/Sn [31, 34], so that a gradual change in those upon gradual substitution of Si by Sn is plausible. This has also been found analogously for the Mg_2(Ge,Sn) system [93]. On the other hand there is a clear disagreement between calculations and experiments on the Si-rich side. One possible reason is that our, but also previous[32, 92] DFT calculations yield the band structure at 0 K, while the experimental results are obtained at room temperature. An increase of the density of states effective mass at higher temperatures has been shown e.g. for Mg_2Si [10, 94]. Furthermore Heller et al. showed a quite significant change of m_D^* below room temperature [72]. They furthermore deduced $m_D^* = 2.2\ m_0$ between 200 K and 300 K, however, based on the assumption of optical mode and impurity scattering, which is not supposed to be dominant at room temperature or above [30]. Experimentally a strongly temperature dependent band structure has been deduced for Mg_2Ge recently [95]. A further possible explanation for the observed discrepancy is that the experimental results are based on the assumption of a single parabolic band which might not be well fulfilled, firstly as Mg_2(Si,Sn) has three bands that contribute to the thermoelectric transport and secondly these bands are not strictly parabolic [32], see also [93] for the Mg_2(Ge,Sn) system. However, the SPB model has been applied successfully to complex band structures before [62] and none of the mentioned points necessarily explains why there is good agreement on the Sn-rich side, but not at the Si-rich side.

While a large density of states effective mass is beneficial for a high Seebeck coefficient, a low effective mass is beneficial for the power factor of systems where electronic transport is governed by acoustic phonon scattering [27]. As all solid solutions of Mg_2(Si,Sn) have a comparable valence band structure this implies, that Sn-rich solid solutions will have a power factor superior to their Si-rich counterparts, and, as the thermal conductivity of both binaries are comparable, this holds for the thermoelectric figure of merit as well. This is independent of the low dopant efficiencies found for Si-rich solutions and would presumably still hold if that could be overcome by e.g. a new dopant. Note however, that the band gap decreases with increasing Sn content, leading to a stronger (negative)

influence of the minority carriers on the thermoelectric performance for Sn-rich solid solutions. The actual optimum composition for p-type $Mg_2(Si,Sn)$ therefore depends also on the minority carrier properties and the considered temperature range.

With respect to the effective mass of individual bands we find that the heavy band is by far dominant for all compositions, in agreement with the results in [32, 34]. In [34] the transport effective masses in certain crystallographic directions were calculated which is not directly comparable to the DOS effective mass. We obtain a quite large band mass ratio ($m^*_{D,HH}/m^*_{D,LH} \approx 3.4$ for Mg_2Si and Mg_2Sn), larger than what is used in previous works to model experimental data. Bakh et al. used $m^*_{D,HH}/m^*_{D,LH} = 1.5m_0/1m_0$ for the full solid solution range while Satyala and Vashaee used $m^*_{D,HH}/m^*_{D,LH} = 2m_0/1m_0$ to model Mg_2Si. Disagreement is not surprising here as the values in the publications were not obtained independently, but rather as a result of a multi-parameter model to fit few experimental data sets. This rather indicates the need for an independent source of the band effective mass values to improve multiband modeling approaches and enhance their predictive power.

Conclusion

We have calculated and compared experimental results for the valence band density of states effective mass for Mg_2Si, Mg_2Sn and their solid solution. The experimental data was obtained from measured transport data assuming the validity of a single parabolic band model, while the calculated results were obtained directly from the density of states employing meta-GGA DFT. Our own experimental data is consistent with previous results and the calculation results are self-consistent with respect to the cell size if the lift of degeneracy of the valence band is correctly taken into consideration. Furthermore both experimental and calculated results show an increase of the density of states effective mass from Mg_2Sn to Mg_2Si and they also agree with each other for Sn-rich solid solutions. For Si-rich solutions there is a clear disagreement, possible reasons for that are discussed but further investigations are required. Better and more reliable knowledge on the density of states effective mass allows for a better modeling of the thermoelectric transport properties in this material class and hence for a more efficient material optimization.

Supporting Information: Validation of the applicability of a single parabolic band model for the analysis of the low doped samples; further calculated material properties; discussion of the artificial lift of the VB band degeneracy in P222 calculations; discussion of the effect of Li on the band structure; comparison of exchange correlation functionals

Acknowledgements

H. Kamila and V. K. Galwadu Arachchige are acknowledged for their support with sample preparation as well as preliminary data analysis. J. de Boor and P. Jund wish to acknowledge the endorsement from the DLR Executive Board Member for Space Research and Technology and the financial support from the Young Research Group Leader Program. J. de Boor also acknowledges support by the

Deutsche Forschungsgemeinschaft (DFG, German Research Foundation) - project number 396709363.

TOC graphic

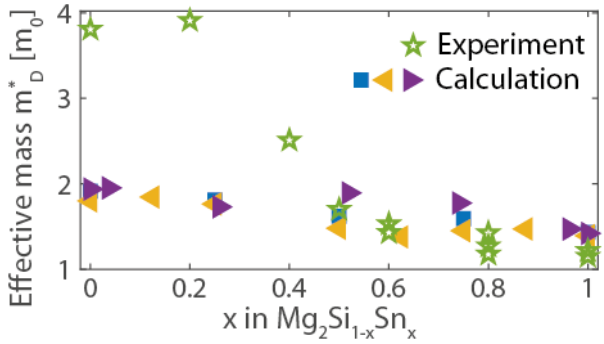

References

1. Bell, L. E., Cooling, Heating, Generating Power, and Recovering Waste Heat with Thermoelectric Systems. *Science* **2008**, *321*, 1457.
2. He, W.; Zhang, G.; Zhang, X.; Ji, J.; Li, G.; Zhao, X., Recent development and application of thermoelectric generator and cooler. *Appl Energ* **2015**, *143*, 1.
3. Hu, X.; Jood, P.; Ohta, M.; Kunii, M.; Nagase, K.; Nishiate, H.; Kanatzidis, M. G.; Yamamoto, A., Power generation from nanostructured PbTe-based thermoelectrics: comprehensive development from materials to modules. *Energ Environ Sci* **2016**, *9*, 517.
4. Qiu, Y. T., et al., Charge-Compensated Compound Defects in Ga-containing Thermoelectric Skutterudites. *Adv. Funct. Mater.* **2013**, *23*, 3194.
5. Yan, X. A., et al., Enhanced Thermoelectric Figure of Merit of p-Type Half-Heuslers. *Nano Lett.* **2011**, *11*, 556.
6. Zhang, J.; Song, L.; Pedersen, S. H.; Yin, H.; Hung, L. T.; Iversen, B. B., Discovery of high-performance low-cost n-type Mg3Sb2-based thermoelectric materials with multi-valley conduction bands. *Nat Commun* **2017**, *8*, 13901.
7. Liu, W.; Tan, X. J.; Yin, K.; Liu, H. J.; Tang, X. F.; Shi, J.; Zhang, Q. J.; Uher, C., Convergence of Conduction Bands as a Means of Enhancing Thermoelectric Performance of n-Type Mg2Si1-xSnx Solid Solutions. *Phys. Rev. Lett.* **2012**, *108*, 166601.
8. Bux, S. K.; Yeung, M. T.; Toberer, E. S.; Snyder, G. J.; Kaner, R. B.; Fleurial, J. P., Mechanochemical synthesis and thermoelectric properties of high quality magnesium silicide. *J. Mater. Chem.* **2011**, *21*, 12259.
9. de Boor, J.; Compere, C.; Dasgupta, T.; Stiewe, C.; Kolb, H.; Schmitz, A.; Mueller, E., Fabrication parameters for optimized thermoelectric Mg2Si. *J Mater Sci* **2014**, *49*, 3196.
10. de Boor, J.; Dasgupta, T.; Kolb, H.; Compere, C.; Kelm, K.; Mueller, E., Microstructural effects on thermoelectric efficiency: A case study on magnesium silicide. *Acta Mater.* **2014**, *77*, 68.
11. Tani, J.-I.; Kido, H., Thermoelectric properties of Al-doped Mg2Si1-xSnx (x <= 0.1). *J. Alloys Compd.* **2008**, *466*, 335.
12. Tani, J.-I.; Kido, H., Thermoelectric properties of Sb-doped Mg2Si semiconductors. *Intermetallics* **2007**, *15*, 1202.

13. Sankhla, A.; Patil, A.; Kamila, H.; Yasseri, M.; Farahi, N.; Mueller, E.; de Boor, J., Mechanical Alloying of Optimized Mg2(Si,Sn) Solid Solutions: Understanding Phase Evolution and Tuning Synthesis Parameters for Thermoelectric Applications. *ACS Appl Energ Mat* **2018**, *1*, 531.
14. Jacobsen, M. K.; Liu, W.; Li, B., Measurement setup for the simultaneous determination of diffusivity and Seebeck coefficient in a multi-anvil apparatus. *Rev Sci Instrum* **2012**, *83*, 093903.
15. LeBlanc, S.; Yee, S. K.; Scullin, M. L.; Dames, C.; Goodson, K. E., Material and manufacturing cost considerations for thermoelectrics. *Renew. Sust. Energ. Rev.* **2014**, *32*, 313.
16. Gaultois, M. W.; Sparks, T. D.; Borg, C. K. H.; Seshadri, R.; Bonificio, W. D.; Clarke, D. R., Data-Driven Review of Thermoelectric Materials: Performance and Resource Considerations. *Chem. Mater.* **2013**, *25*, 2911.
17. de Boor, J.; Dasgupta, T.; Mueller, E., Thermoelectric Properties of Magnesium Silicide Based Solid Solutions and Higher Manganese Silicides. In *Materials Aspect of Thermoelectricty*, Uher, C., Ed. Taylor & Francis: 2016.
18. Goyal, G. K.; Mukherjee, S.; Mallik, R. C.; Vitta, S.; Samajdar, I.; Dasgupta, T., High Thermoelectric Performance in Mg2(Si0.3Sn0.7) by Enhanced Phonon Scattering. *ACS Appl Energ Mat* **2019**, *2*, 2129.
19. Zaitsev, V. K.; Fedorov, M. I.; Gurieva, E. A.; Eremin, I. S.; Konstantinov, P. P.; Samunin, A. Y.; Vedernikov, M. V., Highly effective Mg2Si1-xSnx thermoelectrics. *Phys. Rev. B* **2006**, *74*, 045207.
20. Kamila, H.; Sahu, P.; Sankhla, A.; Yasseri, M.; Pham, H.-N.; Dasgupta, T.; Mueller, E.; de Boor, J., Analyzing transport properties of p-type Mg2Si–Mg2Sn solid solutions: optimization of thermoelectric performance and insight into the electronic band structure. *Journal of Materials Chemistry A* **2019**, *7*, 1045.
21. de Boor, J.; Dasgupta, T.; Saparamadu, U.; Müller, E.; Ren, Z. F., Recent progress in p-type thermoelectric magnesium silicide based solid solutions. *Materials Today Energy* **2017**, *4*, 105.
22. Saparamadu, U.; de Boor, J.; Mao, J.; Song, S.; Tian, F.; Liu, W.; Zhang, Q.; Ren, Z., Comparative studies on thermoelectric properties of p-type Mg2Sn0.75Ge0.25 doped with lithium, sodium, and gallium. *Acta Mater.* **2017**, *141*, 154.
23. de Boor, J.; Saparamadu, U.; Mao, J.; Dahal, K.; Müller, E.; Ren, Z., Thermoelectric performance of Li doped, p-type Mg2(Ge,Sn) and comparison with Mg2(Si,Sn). *Acta Mater.* **2016**, *120*, 273.
24. Fu, C., et al., Revealing the Intrinsic Electronic Structure of 3D Half-Heusler Thermoelectric Materials by Angle-Resolved Photoemission Spectroscopy. *Adv Sci* **2020**, *7*, 1902409.
25. Vazquez, F.; Forman, R. A.; Cardona, M., Electroreflectance Measurements on Mg2Si, Mg2Ge, and Mg2Sn. *Physical Review* **1968**, *176*, 905.
26. Isachenko, G. N.; Zaĭtsev, V. K.; Fedorov, M. I.; Burkov, A. T.; Gurieva, E. A.; Konstantinov, P. P.; Vedernikov, M. V., Kinetic properties of p-Mg2Si x Sn1 − x solid solutions for x < 0.4. *Phys Solid State* **2009**, *51*, 1796.
27. Zhang, Q.; Cheng, L.; Liu, W.; Zheng, Y.; Su, X.; Chi, H.; Liu, H.; Yan, Y.; Tang, X.; Uher, C., Low effective mass and carrier concentration optimization for high performance p-type Mg2(1-x)Li2xSi0.3Sn0.7 solid solutions. *PCCP* **2014**, *16*, 23576.
28. Kamila, H.; Goyal, G. K.; Sankhla, A.; Ponnusamy, P.; Mueller, E.; Dasgupta, T.; de Boor, J., Systematic analysis of the interplay between synthesis route, microstructure, and

thermoelectric performance in p-type Mg2Si0.2Sn0.8. *Materials Today Physics* **2019**, 100133.
29. Bahk, J. H.; Bian, Z. X.; Shakouri, A., Electron transport modeling and energy filtering for efficient thermoelectric Mg2Si1-xSnx solid solutions. *Phys. Rev. B* **2014**, *89*, 075204.
30. Pshenai-Severin, D. A.; Fedorov, M. I.; Samunin, A. Y., The Influence of Grain Boundary Scattering on Thermoelectric Properties of Mg2Si and Mg2Si0.8Sn0.2. *J. Electron. Mater.* **2013**, *42*, 1707.
31. Bourgeois, J.; Tobola, J.; Wiendlocha, B.; Chaput, L.; Zwolenski, P.; Berthebaud, D.; Recour, Q.; Gascoin, F.; Scherrer, H., Study of electron, phonon and crystal stability versus thermoelectric properties in Mg2X(X = Si, Sn) compounds and their alloys. *Functional Materials Letters* **2013**, *06*, 1340005.
32. Kutorasinski, K.; Wiendlocha, B.; Tobola, J.; Kaprzyk, S., Importance of relativistic effects in electronic structure and thermopower calculations for Mg2Si, Mg2Ge, and Mg2Sn. *Phys. Rev. B* **2014**, *89*, 115205.
33. Pulikkotil, J. J.; Singh, D. J.; Auluck, S.; Saravanan, M.; Misra, D. K.; Dhar, A.; Budhani, R. C., Doping and temperature dependence of thermoelectric properties in Mg2(Si,Sn). *Phys. Rev. B* **2012**, *86*, 155204.
34. Guerra, J. M.; Mahr, C.; Giar, M.; Czerner, M.; Heiliger, C., Ab initio calculations of electronic band structure and effective-mass parameters of thermoelectric Mg2X1-xYx(X, Y = Si, Ge, or Sn) pseudobinary alloys. *Phys. Rev. Mater.* **2018**, *2*, 8.
35. Andersen, H. L.; Zhang, J.; Yin, H.; Iversen, B. B., Structural stability and thermoelectric properties of cation- and anion-doped Mg2Si0.4Sn0.6. *Inorganic Chemistry Frontiers* **2017**, *4*, 456.
36. Kamila, H.; Sankhla, A.; Yasseri, M.; Hoang, N. P.; Farahi, N.; Mueller, E.; de Boor, J., Synthesis of p-type Mg2Si1-xSnx with x = 0-1 and optimization of the synthesis parameters. *Materials Today: Proceedings* **2019**, *8*, 546.
37. Yasseri, M.; Schüpfer, D.; Chen, L.; Kamila, H.; Müller, E.; de Boor, J.; Klar, P. J., Raman Spectroscopic Study of the Optical Phonons of Mg2Si1-xSnx Solid Solutions. *Phys Status Solidi-R* **2020**, *14*, 6.
38. Madsen, G. K. H.; Singh, D. J., BoltzTraP. A code for calculating band-structure dependent quantities. *Comput. Phys. Commun.* **2006**, *175*, 67.
39. Viennois, R.; Colinet, C.; Jund, P.; Tédenac, J.-C., Phase stability of ternary antifluorite type compounds in the quasi-binary systems Mg2X–Mg2Y (X, Y = Si, Ge, Sn) via ab-initio calculations. *Intermetallics* **2012**, *31*, 145.
40. Yasseri, M.; Sankhla, A.; Kamila, H.; Orenstein, R.; Truong, D. Y. N.; Farahi, N.; de Boor, J.; Mueller, E., Solid solution formation in Mg2(Si,Sn) and shape of the miscibility gap. *Acta Mater.* **2020**, *185*, 80.
41. Gao, H. L.; Zhu, T. J.; Liu, X. X.; Chen, L. X.; Zhao, X. B., Flux synthesis and thermoelectric properties of eco-friendly Sb doped Mg2Si0.5Sn0.5 solid solutions for energy harvesting. *J. Mater. Chem.* **2011**, *21*, 5933.
42. Liu, J.-W.; Song, M.; Takeguchi, M.; Tsujii, N.; Isoda, Y., Transmission Electron Microscopy Study of Mg2Si0.5Sn0.5 Solid Solution for High-Performance Thermoelectrics. *J. Electron. Mater.* **2015**, *44*, 407.
43. Yi, S.-i.; Attari, V.; Jeong, M.; Jian, J.; Xue, S.; Wang, H.; Arroyave, R.; Yu, C., Strain-induced suppression of the miscibility gap in nanostructured Mg2Si–Mg2Sn solid solutions. *Journal of Materials Chemistry A* **2018**, *6*, 17559.

44. de Boor, J.; Stiewe, C.; Ziolkowski, P.; Dasgupta, T.; Karpinski, G.; Lenz, E.; Edler, F.; Mueller, E., High-Temperature Measurement of Seebeck Coefficient and Electrical Conductivity. *J. Electron. Mater.* **2013**, *42*, 1711.
45. de Boor, J.; Muller, E., Data analysis for Seebeck coefficient measurements. *Rev. Sci. Instrum.* **2013**, *84*, 065102.
46. Borup, K. A., et al., Measuring thermoelectric transport properties of materials. *Energ Environ Sci* **2015**, *8*, 423.
47. van der Pauw, L. J., A method of measuring specific resistivity and Hall effect of discs of arbitrary shape. *Philips Res. Rep.* **1958**, *13*, 1.
48. Wang, H. S., et al., International Round-Robin Study of the Thermoelectric Transport Properties of an n-Type Half-Heusler Compound from 300 K to 773 K. *J. Electron. Mater.* **2015**, *44*, 4482.
49. Ziolkowski, P.; Stiewe, C.; de Boor, J.; Druschke, I.; Zabrocki, K.; Edler, F.; Haupt, S.; König, J.; Mueller, E., Iron Disilicide as High-Temperature Reference Material for Traceable Measurements of Seebeck Coefficient Between 300 K and 800 K. *J. Electron. Mater.* **2017**, *46*, 51.
50. Kolb, H.; Dasgupta, T.; Zabrocki, K.; Mueller, E.; de Boor, J., Simultaneous measurement of all thermoelectric properties of bulk materials in the temperature range 300–600 K. *Rev. Sci. Instrum.* **2015**, *86*, 073901.
51. Kresse, G.; Furthmüller, J., Efficiency of ab-initio total energy calculations for metals and semiconductors using a plane-wave basis set. *Computational Materials Science* **1996**, *6*, 15.
52. Kresse, G.; Furthmüller, J., Efficient iterative schemes for ab initio total-energy calculations using a plane-wave basis set. *Phys. Rev. B* **1996**, *54*, 11169.
53. Kresse, G.; Joubert, D., From ultrasoft pseudopotentials to the projector augmented-wave method. *Phys. Rev. B* **1999**, *59*, 1758.
54. Blöchl, P. E., Projector augmented-wave method. *Phys. Rev. B* **1994**, *50*, 17953.
55. Perdew, J. P.; Wang, Y., Accurate and simple analytic representation of the electron-gas correlation energy. *Phys. Rev. B* **1992**, *45*, 13244.
56. Ryu, B.; Park, S.; Choi, E.-A.; de Boor, J.; Ziolkowski, P.; Chung, J.; Park, S. D., Hybrid-Functional and Quasi-Particle Calculations of Band Structures of Mg2Si, Mg2Ge, and Mg2Sn. *J Kor Phys Soc* **2019**, *75*, 144.
57. Becke, A. D.; Johnson, E. R., A simple effective potential for exchange. *The Journal of Chemical Physics* **2006**, *124*, 221101.
58. Tran, F.; Blaha, P., Accurate Band Gaps of Semiconductors and Insulators with a Semilocal Exchange-Correlation Potential. *Phys. Rev. Lett.* **2009**, *102*, 226401.
59. Zunger, A.; Wei, S. H.; Ferreira, L. G.; Bernard, J. E., Special quasirandom structures. *Phys. Rev. Lett.* **1990**, *65*, 353.
60. van de Walle, A.; Tiwary, P.; de Jong, M.; Olmsted, D. L.; Asta, M.; Dick, A.; Shin, D.; Wang, Y.; Chen, L. Q.; Liu, Z. K., Efficient stochastic generation of special quasirandom structures. *Calphad* **2013**, *42*, 13.
61. May, A. F.; Snyder, G. J., Introduction to Modeling Thermoelectric Transport at High Temperatures. In *Thermoelectrics and its Energy Harvesting: Materials, Preparation, and Characterization in Thermoelectrics*, Rowe, D. M., Ed. CRC Press: 2012.
62. Liu, W.; Chi, H.; Sun, H.; Zhang, Q.; Yin, K.; Tang, X.; Zhang, Q.; Uher, C., Advanced thermoelectrics governed by a single parabolic band: Mg2Si(0.3)Sn(0.7), a canonical example. *Phys Chem Chem Phys* **2014**, *16*, 6893.

63. Liu, X.; Xi, L.; Qiu, W.; Yang, J.; Zhu, T.; Zhao, X.; Zhang, W., Significant Roles of Intrinsic Point Defects in Mg2X(X= Si, Ge, Sn) Thermoelectric Materials. *Adv. Electron. Mater.* **2016**, *2*, 1500284.
64. Han, X. P.; Shao, G. S., Interplay between Ag and interstitial Mg on the p-type characteristics of Ag-doped Mg2Si: challenges for high hole conductivity. *J. Mater. Chem. C* **2015**, *3*, 530.
65. Jund, P.; Viennois, R.; Colinet, C.; Hug, G.; Fevre, M.; Tedenac, J. C., Lattice stability and formation energies of intrinsic defects in Mg2Si and Mg2Ge via first principles simulations. *J Phys Condens Matter* **2013**, *25*, 035403.
66. Viennois, R.; Jund, P.; Colinet, C.; Tedenac, J. C., Defect and phase stability of solid solutions of Mg2X with an antifluorite structure: An ab initio study. *J. Solid State Chem.* **2012**, *193*, 133.
67. Sondergaard, M.; Christensen, M.; Borup, K. A.; Yin, H.; Iversen, B. B., Thermoelectric Properties of the Entire Composition Range in Mg2Si0.9925-x Sn (x) Sb-0.0075. *J. Electron. Mater.* **2013**, *42*, 1417.
68. Chen, L. X.; Jiang, G. Y.; Chen, Y.; Du, Z. L.; Zhao, X. B.; Zhu, T. J.; He, J.; Tritt, T. M., Miscibility gap and thermoelectric properties of ecofriendly Mg2Si1-xSnx (0.1 <= x <= 0.8) solid solutions by flux method. *J. Mater. Res.* **2011**, *26*, 3038.
69. Brahim, M.; Hamza, L.; Lagoun, B.; Khemakhem, H. In *The DFT (TB-mBJ) calculation of structural, electronic, elastic and vibrational properties of Mg2X(X=Si,Sn)*, Hammamet, 22 - 24 03. 2017; 2017.
70. Yan, X.-Y.; Chang, Y. A.; Zhang, F., A thermodynamic analysis of the Mg-Si system. *Journal of Phase Equilibria* **2000**, *21*, 379.
71. Yuan, X.; Sun, W.; Du, Y.; Zhao, D.; Yang, H., Thermodynamic modeling of the Mg–Si system with the Kaptay equation for the excess Gibbs energy of the liquid phase. *Calphad* **2009**, *33*, 673.
72. Heller, M. W.; Danielson, G. C., Seebeck effect in Mg2Si single crystals. *J. Phys. Chem. Solids* **1962**, *23*, 601.
73. Stella, A.; Lynch, D. W., Photoconductivity in Mg2Si and Mg2Ge. *J. Phys. Chem. Solids* **1964**, *25*, 1253.
74. Nakagawa, R.; Katsumata, H.; Hashimoto, S.; Sakuragi, S., Synthesis and crystal growth of Mg2Si by the liquid encapsulated vertical gradient freezing method. *Jpn. J. Appl. Phys.* **2015**, *54*, 085503.
75. Zaitsev, V. K.; Federov, M. I.; Eremin, I. S.; Gurieva, E. A., Thermoelectrics on the Base of Solid Solutions of Mg2B IVCompounds. In *Thermoelectrics Handbook: Macro to Nano*, Rowe, D. M., Ed. CRC: Boca Raton, USA, 2005.
76. Jung, I. H.; Kang, D. H.; Park, W. J.; Kim, N. J.; Ahn, S., Thermodynamic modeling of the Mg-Si-Sn system. *Calphad* **2007**, *31*, 192.
77. Winkler, U. E. Die elektrischen Eigenschaften der intermetallischen Verbindungen Mg2Si, Mg2Ge, Mg2Sn und Mg2Pb. Eidgenoessische Technische Hochschule in Zuerich, Buchdruckerei Birkhäuser AG, Basel, 1955.
78. Blunt, R. F.; Frederikse, H. P. R.; Hosler, W. R., Electrical and Optical Properties of Intermetallic Compounds. IV. Magnesium Stannide. *Physical Review* **1955**, *100*, 663.
79. Lawson, W. D.; Nielsen, S.; Putley, E. H.; Roberts, V., XXV. The Preparation, Electrical and Optical Properties of Mg2Sn. *Journal of Electronics and Control* **1955**, *1*, 203.
80. Lipson, H. G.; Kahan, A., Infrared Absorption of Magnesium Stannide. *Physical Review* **1964**, *133*, A800.
81. Boulet, P.; Record, M. C., Influence of the modified Becke-Johnson exchange potential on thermoelectric properties: Application to Mg2Si. *J. Chem. Phys.* **2011**, *135*, 8.

82. Jin, Y. R.; Feng, Z. Z.; Ye, L. Y.; Yan, Y. L.; Wang, Y. X., Mg2Sn: a potential mid-temperature thermoelectric material. *RSC Adv.* **2016**, *6*, 48728.
83. Wiendlocha, B., Thermopower of thermoelectric materials with resonant levels: PbTe:Tl versus PbTe:Na and Cu1−xNix. *Phys. Rev. B* **2018**, *97*, 205203.
84. Gao, P.; Davis, J. D.; Poltavets, V. V.; Hogan, T. P., The p-type Mg2LixSi0.4Sn0.6 thermoelectric materials synthesized by a B2O3 encapsulation method using Li2CO3 as the doping agent. *J. Mater. Chem. C* **2016**, *4*, 929.
85. Isachenko, G. N.; Samunin, A. Y.; Gurieva, E. A.; Fedorov, M. I.; Pshenay-Severin, D. A.; Konstantinov, P. P.; Kamolova, M. D., Thermoelectric Properties of Nanostructured p-Mg2SixSn1-x (x=0.2 to 0.4) Solid Solutions. *J. Electron. Mater.* **2016**, *45*, 1982.
86. Tan, X. J.; Liu, W.; Liu, H. J.; Shi, J.; Tang, X. F.; Uher, C., Multiscale calculations of thermoelectric properties of n-type Mg2Si1−xSnx solid solutions. *Phys. Rev. B* **2012**, *85*.
87. Satyala, N.; Vashaee, D., Modeling of Thermoelectric Properties of Magnesium Silicide (Mg2Si). *J. Electron. Mater.* **2012**, *41*, 1785.
88. Zhang, L.; Xiao, P.; Shi, L.; Henkelman, G.; Goodenough, J. B.; Zhou, J., Suppressing the bipolar contribution to the thermoelectric properties of Mg2Si0.4Sn0.6 by Ge substitution. *J. Appl. Phys.* **2015**, *117*, 155103.
89. Ihou-Mouko, H.; Mercier, C.; Tobola, J.; Pont, G.; Scherrer, H., Thermoelectric properties and electronic structure of p-type Mg2Si and Mg2Si0.6Ge0.4 compounds doped with Ga. *J. Alloys Compd.* **2011**, *509*, 6503.
90. Fedorov, M. I.; Zaĭtsev, V. K.; Eremin, I. S.; Gurieva, E. A.; Burkov, A. T.; Konstantinov, P. P.; Vedernikov, M. V.; Samunin, A. Y.; Isachenko, G. N.; Shabaldin, A. A., Transport properties of Mg2 X 0.4Sn0.6 solid solutions (X = Si, Ge) with p-type conductivity. *Phys Solid State* **2006**, *48*, 1486.
91. Liu, W.; Yin, K.; Su, X.; Li, H.; Yan, Y.; Tang, X.; Uher, C., Enhanced hole concentration through Ga doping and excess of Mg and thermoelectric properties of p-type Mg2(1+z)(Si0.3Sn0.7)(1-y)Ga-y. *Intermetallics* **2013**, *32*, 352.
92. Shi, G.; Kioupakis, E., Relativistic quasiparticle band structures of Mg2Si, Mg2Ge, and Mg2Sn: Consistent parameterization and prediction of Seebeck coefficients. *J. Appl. Phys.* **2018**, *123*, 085114.
93. Sun, J.; Singh, D. J., Thermoelectric Properties ofMg2(Ge,Sn): Model and Optimization of ZT. *Phys. Rev. Appl.* **2016**, *5*, 024006.
94. Bux, S. K.; Blair, R. G.; Gogna, P. K.; Lee, H.; Chen, G.; Dresselhaus, M. S.; Kaner, R. B.; Fleurial, J.-P., Nanostructured Bulk Silicon as an Effective Thermoelectric Material. *Adv. Funct. Mater.* **2009**, *19*, 2445.
95. Kamila, H.; Sankhla, A.; Yasseri, M.; Mueller, E.; de Boor, J., Non-Rigid Band Structure in Mg2Ge for Improved Thermoelectric Performance. *Advanced Science* **2020**, *n/a*, 2000070.